ACS NANO

www.acsnano.org

Fabrication of Centimeter-Scale Plasmonic Nanoparticle Arrays with Ultranarrow Surface Lattice Resonances

Fan Yang,[‖] Qianyun Chen,[‖] Jiajun Wang, Julia J. Chang, Wenhao Dong, Wei Cao, Shunsheng Ye, Lei Shi,[*] and Zhihong Nie[*]

Cite This: *ACS Nano* 2023, 17, 725−734

Read Online

ACCESS | Metrics & More | Article Recommendations | Supporting Information

ABSTRACT: **Plasmonic surface lattice resonances (SLRs) supported by metallic nanoparticle (NP) arrays show diverse applications including nanolasers, sensors, photocatalysis, and nonlinear optics. However, to rationally fabricate high-quality plasmonic NP arrays with ultranarrow SLR line widths over large areas remains challenging. This article describes a general approach for the efficient fabrication of centimeter-scale inorganic NP arrays with precisely controlled NP size, composition, position, and lattice geometry. This method combines the processes of solvent-assisted soft lithography and in situ site-specific NP growth to reproducibly create many replicates of NP arrays without utilizing cleanroom and specialized equipment. For demonstration, we show that Au NP arrays exhibit ultranarrow SLRs with a line width of 4 nm and a quality factor of 218 toward the theoretical limit.**

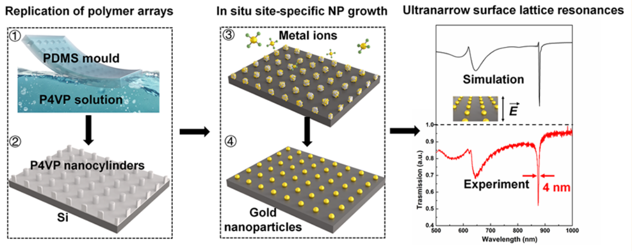

KEYWORDS: *inorganic nanoparticles, arrays, bottom-up, plasmonic, surface lattice resonance*

Inorganic nanoparticles (NPs), such as plasmonic, magnetic, and semiconductor particles, have attracted great attention, owing to their intrinsic optical, magnetic, electronic, chemical, and catalytic properties.[1−5] Among others, plasmonic NPs are one of the most powerful platforms for controlling light−matter interactions. Plasmonic nanostructures can efficiently couple light into nanostructures and squeeze light into subwavelength volumes, due to the so-called localized surface plasmon resonance (LSPR).[6] These localized excitations accompanied by large near-field enhancement have enabled enormous applications of plasmonic NPs in sensing,[7,8] nanophotonics,[9,10] photochemistry,[11] and nonlinear optics.[12] However, the strong energy loss mainly in radiative mode (i.e., the conversion of plasmons into photons) within individual plasmonic NPs results in broadband resonances (typical fwhm >80 nm) with a low quality-factor (Q-factor), severely limiting the applications of plasmonic NPs in such as nanolasing and sensing.[13−16] It remains challenging to effectively reduce the loss by decreasing the Landau damping (the damping of a collective mode of oscillations without collisions) or the plasmon energy damping originating from electron collisions with other electrons, defects, and phonons.[17]

An efficient way to suppress the radiative losses is to arrange the plasmonic NPs into periodic arrays to achieve a hybrid excitation-surface lattice resonance (SLR).[13,18,19] The SLR modes are coupling modes between the diffraction mode of the array and LSPR mode of a single NP, which supports an ultranarrow plasmon resonance toward the theoretical limit of ∼1−2 nm.[15] Such narrow SLR, however, cannot be readily achieved in experiments, largely because of the difficulty in fabricating precise yet defect-free individual NPs and the arrays. Bottom-up self-assembly templated by nanoscale chemical or topological patterns can be used to arrange wet-chemically synthesized NPs with high uniformity and tunable size and composition into ordered arrays, but the precise level of NP arrangement in the arrays is rather limited.[20−22] The relatively low degree of order is caused by the contradicting requirement on the relative dimension of constituent NPs and nanoscale patterns between high yield and high precision in NP assembly. The interfacial self-assembly approach can produce close-packed NP arrays, but the distance between NPs is too small to achieve the diffraction effect and the SLR

Received: October 13, 2022
Accepted: December 21, 2022
Published: December 28, 2022

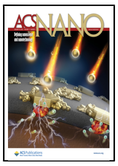

https://doi.org/10.1021/acsnano.2c10205

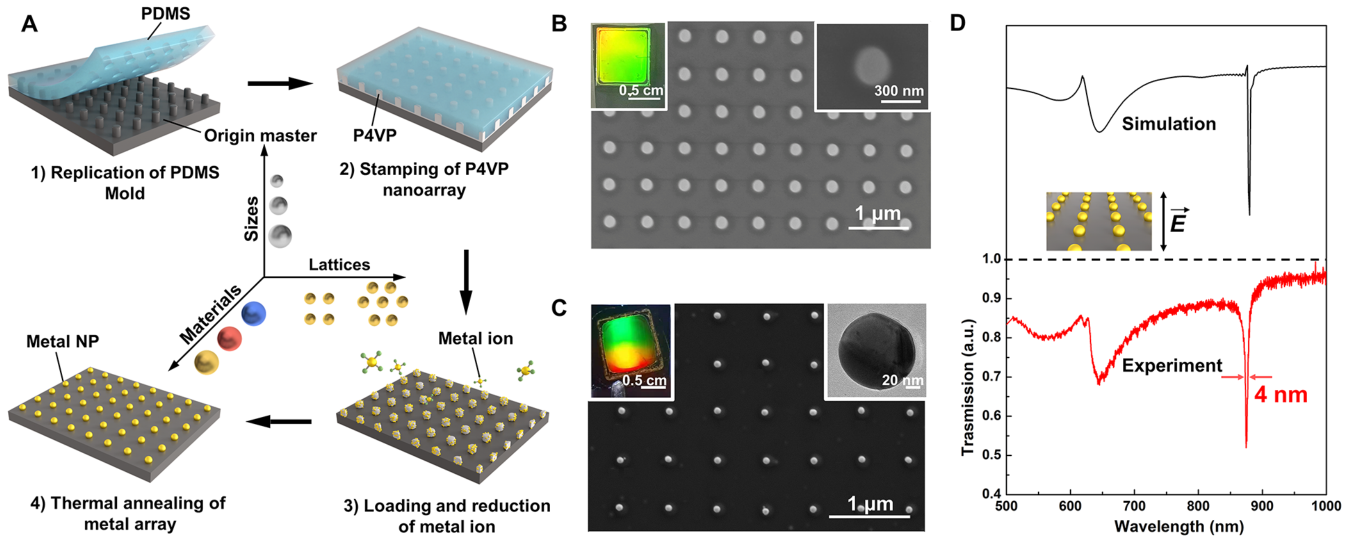

Figure 1. Fabrication of inorganic NP arrays with tunable sizes, compositions, and lattice parameters. (A) Schematic illustration of the nanofabrication process of large-area inorganic NP arrays. (B, C) SEM images of the P4VP nanocylinder array (B) and the GNP array (C). Insets at the left are optical micrographs of the corresponding large-area P4VP nanoarrays (B) and GNP array (C). Insets at the right are SEM images of single P4VP nanocylinder (B) and TEM image of single GNP (C). (D) Simulated and measured transmission spectra of the GNP array under linear polarized light. Inset shows that the incident electric field is aligned along the high-symmetry lattice direction.

mode in the visible and near-infrared range.[23,24] In contrast, a top-down technique based on templated metal deposition is capable of generating gold NP (GNP) arrays with ultranarrow SLR line widths. This approach, however, involves costly, complicated, and time-consuming processes (e.g., fabrication of Au nanohole film by templated metal deposition, masked metal deposition through the nanoholes, and high-temperature thermal annealing), which heavily rely on cleanroom facilities.[15,25−27] Furthermore, metal reduction in nanodomains of block copolymers self-assembled on substrates or patterned by dip-pen nanolithography provides an alternative tool to fabricate arrays of NPs with uniform size and shape.[28−30] This technique, however, is not scalable or shows limited control over the lattice parameters (e.g., periodicity, symmetry, NP size).[31] Nevertheless, there is an urgent need of simple strategies for fabricating large-area NP arrays with high *Q*-factors in a flexible yet precise manner.

Here we present a robust approach for the large-area fabrication of defect-free periodic arrays of highly uniform inorganic NPs with high precision in NP arrangement (Figure 1). This approach is mainly based on the soft lithographic patterning of polymeric nanoarrays for chelating metal precursors, in situ reduction of metals, and thermal annealing of NP arrays. By using this approach, we produce a gallery of NP arrays from metals (e.g., Au, Pd, and Pt), metal alloys of different compositions (e.g., AuPd, FePt, and CoPt), and metal oxides (e.g., Fe_2O_3, CoO_2). The area of the arrays is on the centimeter scale, and the NPs show smooth surface and high uniformity in size and shape. This fabrication method is robust and highly flexible: the size of the NPs can be reproducibly tuned by varying the height of polymer nanoarrays, and the lattice parameters (e.g., geometric symmetry and periodicity of lattices) can be controlled by the templates used. The NP arrays show an extremely high degree of order in the periodic arrangement of NPs with minimal defect, and hence superior optical properties. For demonstration, we show that GNP arrays exhibit ultranarrow SLR resonances with a line width of ∼4 nm and a *Q*-factor of ∼218. The high-quality NP arrays fabricated by this method may find applications in data storage,[32] sensing,[8] catalysis,[33] and metasurface.[34]

RESULTS AND DISCUSSION

Fabrication of GNP Arrays. The approach we developed involves the fabrication of polymeric nanocylinder arrays by soft lithography, loading of inorganic salt precursors into polymeric nanodomains, selective removal of organic compounds and reduction of inorganic salts by oxygen plasma, and thermal annealing of the NP arrays (Figure 1A and see more details in Supporting Information). A relief silicon master with nanopillars (diameter d = 250 nm, height h = 350 nm, pitch a_0 = 600 nm) was molded against elastomeric polydimethylsiloxane (PDMS) to produce soft PDMS stamps (step 1). The PDMS stamps were inked with a solution of poly(4-vinylpyridine) (P4VP) in solvents (e.g., isopropanol) and brought into conformal contact with a substrate to generate periodic nanocylinder arrays (step 2) (Figure 1B). After a brief O_2 plasma descum process, negatively charged metal precursors ($AuCl_4^-$, $PdCl_4^{2-}$, $PtCl_4^{2-}$ or etc.) were loaded into the P4VP nanocylinders through electrostatic interactions between the precursors and the pyridinic nitrogen groups of P4VP. Subsequently, O_2 plasma treatment was used to remove P4VP and reduce metal ions to the zero valence state by the generated free electrons (step 3).[29,35] Finally, the resulting NPs were thermally annealed to yield highly uniform inorganic NP array with high precision in NP arrangement (step 4). The scanning electron microscopy (SEM) image in Figure 1C shows a representative array composed of highly uniform GNPs. The transmission electron microscopy (TEM) image of a single GNP shows its smooth surface and high crystallinity (inset in Figure 1C, right). The structural color of a centimeter-scale array indicates that the overall structure is highly uniform (inset in Figure 1C, left). The GNP array exhibited a SLR line width of ∼4 nm and a *Q*-factor of ∼218, which is approaching the theoretical limit (Figure 1D). The result is in good agreement with our finite-difference time-

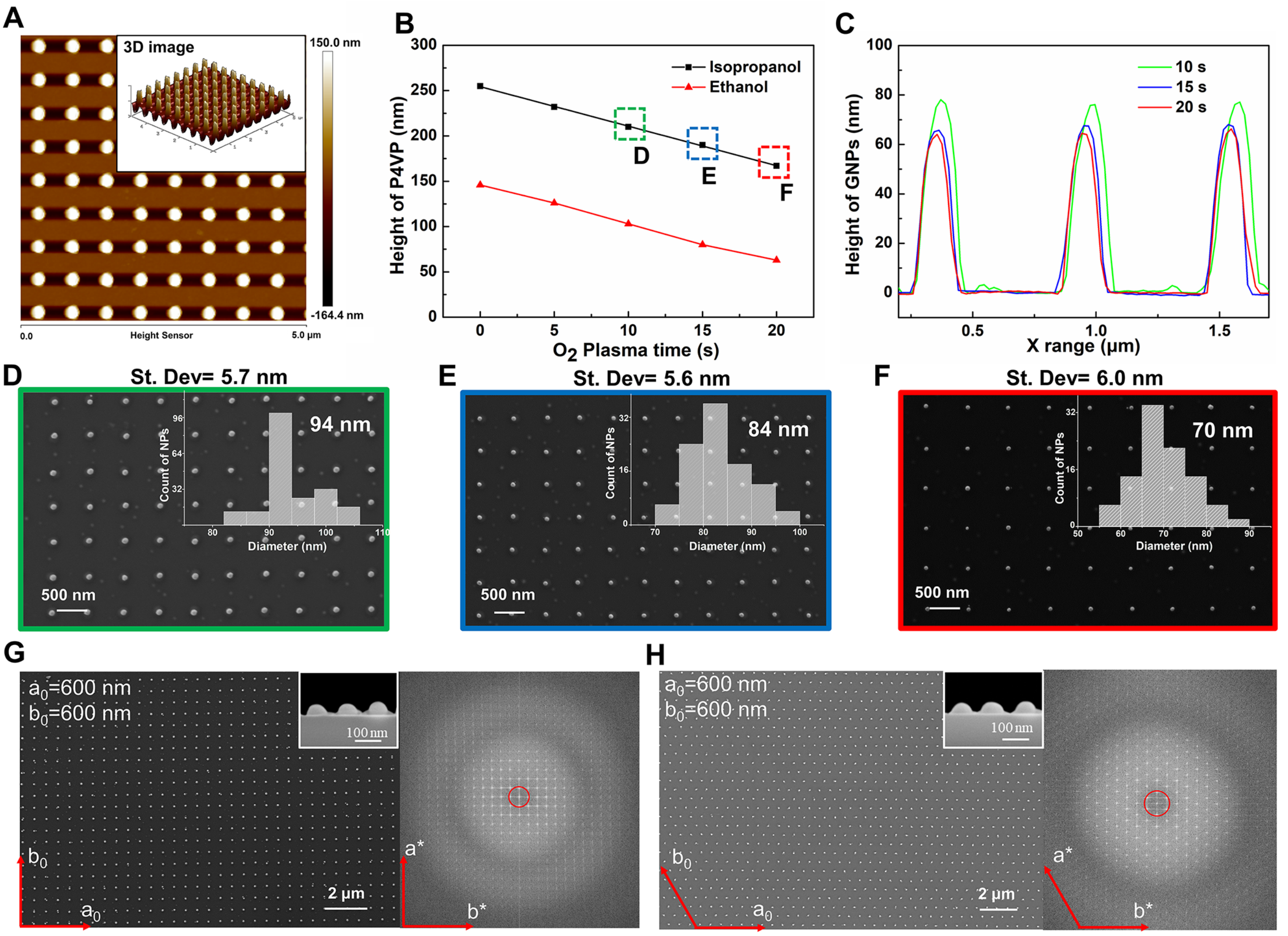

Figure 2. Characterization of large-area GNP array. (A) Tapping-mode 2D and 3D (inset) AFM image of a P4VP nanocylinder array fabricated by soft lithography using isopropanol as solvent. (B) The variation in the height (H_p) of P4VP nanocylinders as a function of O_2 plasma etching time, when isopropanol (black) and ethanol (red) were used as solvents. (C) Height profiles of GNP arrays obtained at different O_2 plasma etching times of P4VP. (D−F) SEM images of GNP arrays with different GNP diameter (D_{NP}) obtained at different O_2 plasma etching times corresponding to the data points in the dashed frames of (B): 10 s (D), 15 s (E), and 20 s (F). Insets are the corresponding size distribution of GNPs. (G, H) Large-area SEM images (left) and corresponding Fast Fourier transform patterns (right) of GNP arrays with different lattice symmetries: square lattice (G) and hexagonal lattice (H). Insets are SEM images of the GNP array at tilted angle of 90°.

domain (FDTD) simulation of the optical response of the GNP array.

During the patterning of P4VP by soft lithography, the solvent swells the PDMS stamp to reduce the dimension of the nanowells, which enables us to generate nanofeatures with dimensions smaller than those of the original silicon master. Thus, the swelling factor, S ($S = L/L_0$, where L_0 and L are the length of PDMS before and after being swollen, respectively) of solvents can be used to tune the dimension of P4VP nanocylinders and hence the diameter (D_{NP}) of resulting inorganic NPs. The atomic force microscopy (AFM) image in Figure 2A shows a representative P4VP nanocylinder array fabricated by using isopropanol ($S = 1.09$) as the solvent. The height (H_p) and diameter of the nanocylinders were ∼255 nm and ∼220 nm, smaller than that of 350 and 250 nm for the silicon master, respectively. The use of solvent with a higher S (e.g., ethanol with $S = 1.11$) resulted in P4VP nanocylinders with a smaller diameter and a lower height (Figure 2B and Figure S1). However, when dichloromethane with $S = 1.22$ was used, the uniformity of the array structures was reduced, probably due to the reduced mechanical property of the stamps. Moreover, the D_{NP} of the GNPs can be accurately controlled by varying H_p of P4VP nanocylinders via oxygen plasma treatment. The increase in the duration of oxygen plasma treatment led to an approximately linear reduction in H_p of P4VP nanocylinders and hence D_{NP} of the GNPs, while not sacrificing the uniformity of the nanostructures (Figure 2B and Figure S2). AFM analysis shows that D_{NP} of the as-fabricated GNPs is slightly smaller than their average height, indicating that the GNPs are not perfect spheres (Figure 2C and Figure S3). When the duration of plasma treatment increased from 10 s, to 15 s, and to 20 s, the H_p of P4VP nanocylinders decreased from 210 ± 1.2 nm, to 190 ± 1.3 nm, and eventually to 167 ± 1.5 nm, respectively. Accordingly, this observation is accompanied by a decrease in D_{NP} of the GNPs from 94 ± 5.7 nm (Figure 2D), to 84 ± 5.6 nm (Figure 2E), and eventually to 70 ± 6.0 nm (Figure 2F), respectively. The small standard deviations of D_{NP} (<9%) confirm the high uniformity of the GNPs. The smallest GNPs obtained by varying plasma etching time had a D_{NP} of ∼40 nm, although

https://doi.org/10.1021/acsnano.2c10205
ACS Nano 2023, 17, 725−734

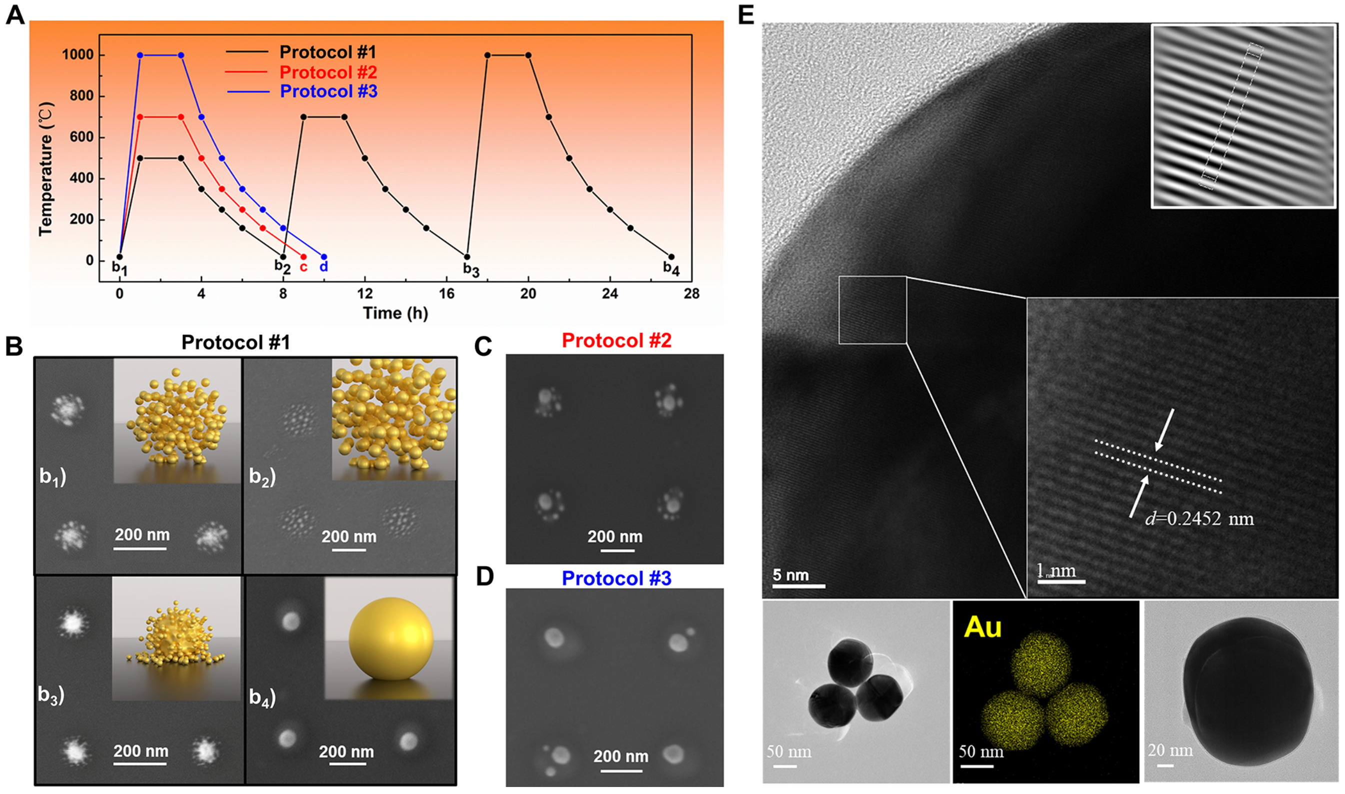

Figure 3. Effect of thermal annealing processes on the formation of single GNP formation. (A) Time-dependent temperature profiles of three different thermal annealing protocols. (B−D) SEM images of GNPs obtained at b_1, b_2, b_3, and b_4 stage of protocol #1 (B), by protocol #2 (C), and protocol #3 (D). Insets are corresponding schematic illustrations of GNPs. (E) HRTEM images, atomic structure of squared region, and EDS map of GNPs. Top-right inset is the lattice fringe.

the long etching process (>20 s) slightly broadened the size distribution of the P4VP nanocylinders and hence the GNPs (Figure S4). We expect that if necessary, the D_{NP} of GNPs can be further decreased by using silicon masters with nanopillars of a smaller diameter or height. Large-area SEM images and corresponding fast Fourier transform (FFT) patterns of square GNP array (Figure 2G) and hexagonal GNP array (Figure 2H) show high precision in the periodic arrangement of monodispersed NPs in the arrays with minimal defects (Figure S5). As shown in SEM images of GNP arrays at tilted angles of 45° and 90°, the GNPs had a dome-like shape, which is in accordance with our AFM measurements (insets in Figure 2G,H and Figure S6). We presume that the GNPs are liquefied and deformed to acquire a nonspherical shape on substrates under gravity during thermal annealing.

Effect of Thermal Annealing. The thermal annealing is crucial to the formation of uniform GNPs with smooth surface and large grain size through the sintering of small NPs or nanoclusters, as demonstrated in a previous publication.[15] The sintering of small GNPs under thermal treatment is governed by two main mechanisms, namely, coalescence sintering and Ostwald ripening sintering.[36] Coalescence sintering occurs when two small GNPs touch or collide and merge into a larger one. In contrast, Ostwald ripening sintering occurs by evaporating and transferring atoms from one GNP to another, which is a dynamic process. To elucidate the mechanism, we compared the formation process of single GNP using three different thermal annealing protocols, as illustrated in Figure 3A. In protocol #1, a cluster of many small GNPs underwent two intermediate states (b_2 and b_3) to finally form a single GNP: a cluster of many small GNPs (b_1) → a more evenly distributed cluster of GNPs (b_2) → core−satellite structure (b_3) → single large GNP (b_4) (Figure 3B and Figure S7). Because the loss rate of small GNPs is higher than large ones, several large GNPs eventually evolved into one single NP at the expense of many small GNPs. In protocol #2 and protocol #3, thermal annealing at a single temperature of 700 or 1000 °C generated one big GNP surrounded by many small GNPs, rather than one single big GNP at one site, largely because of insufficient surface-mediated Ostwald ripening (Figure 3C and 3D). The growth rate (dD_{NP}/dt) of the GNP is inversely proportional to temperature T, following the Wynblatt and Gjostein (W−J) model (see detailed discussions in Supplementary Text S1):[37]

$$dD_{NP}/dt \propto \frac{\gamma\Omega}{kTD_{NP}^{2}}(D_{NP}/D_{NP}^{*} - 1) \quad (1)$$

where t is the annealing time, γ is the surface free energy of the metal, Ω is the volume per atom of the bulk metal, k is Boltzmann's constant, and D_{NP}^* is the reciprocal of ensemble average of $1/D_{NP}$. The growth rate of NPs is slow at a high annealing temperature, thus resulting in the formation of many small NPs, rather than single large NP with a smooth surface and uniform shape, on each site. High-resolution transmission electron microscopy (HRTEM) images revealed that the GNPs were polycrystalline with large grains (Figure 3E). The whole area shows the same average lattice plane spacing of ~0.245 nm, corresponding to the ⟨111⟩ lattice orientation of gold. The grain size within single GNP gradually increased with the progress of thermal annealing because of atom diffusion-induced recrystallization. Based on normal grain

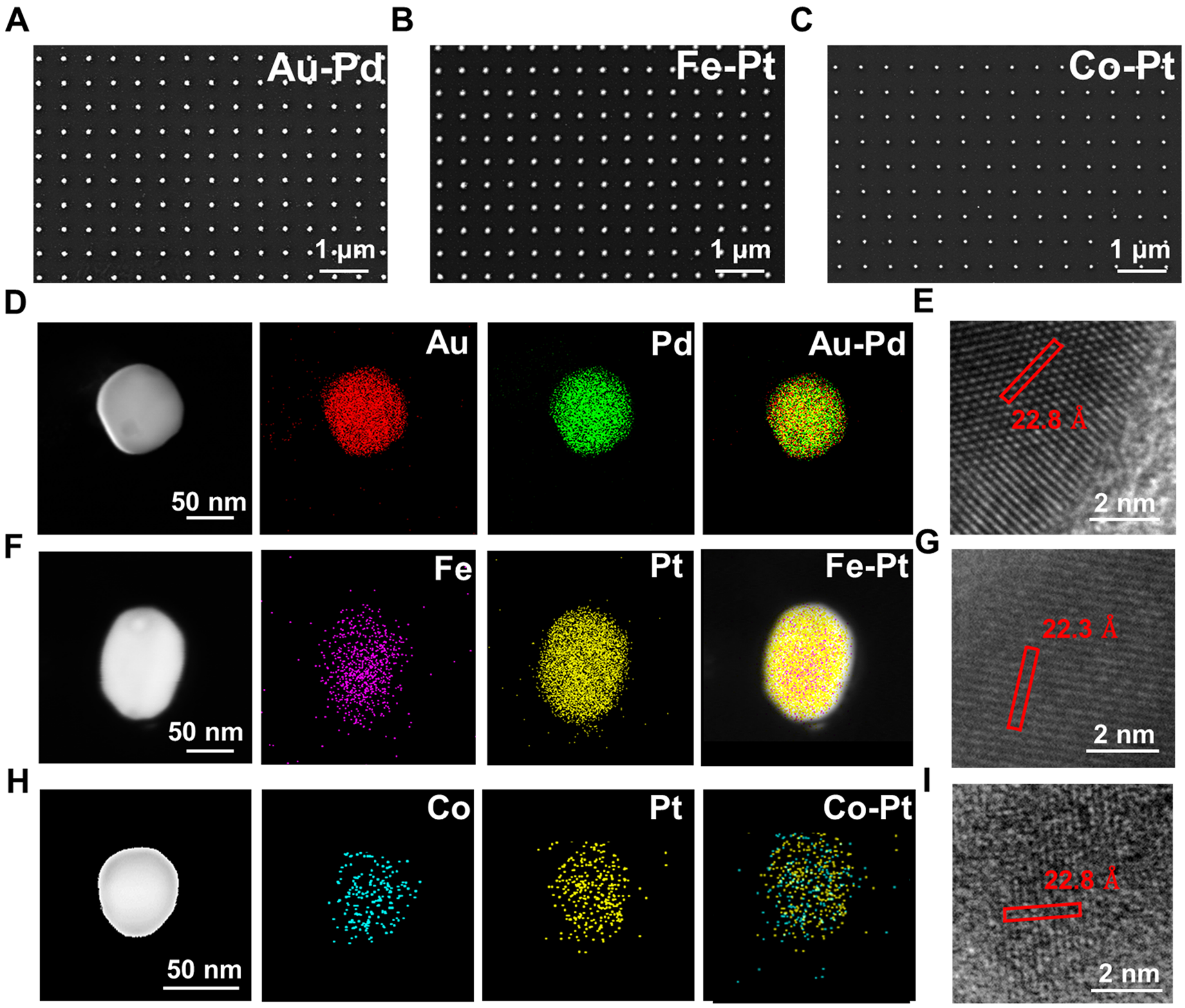

Figure 4. Patterned intermetallic alloy arrays. (A–C) SEM images of different intermetallic alloy arrays: Au–Pd (A), Fe–Pt (B), and Co–Pt (C). (D–I) Representative STEM images and corresponding EDS maps (D, F, H) and HRTEM images (E, G, I) of different intermetallic alloy arrays: Au–Pd (D, E), Fe–Pt (F, G), and Co–Pt NPs (H, I).

growth equation, the average grain size D_g after a time t can be written as[38]

$$D_g^{\ n} - D_{g,0}^n = K_0 t \exp(-E/RT) \quad (2)$$

where $D_{g,0}$ is the initial average grain size, n is the grain growth exponent, K_0 is a constant, E is the activation energy for grain growth, and R is the gas constant. The three-step thermal annealing process in protocol #1 led to a larger grain size of GNPs than that of GNPs obtained through a single-step annealing at 900 °C, which is favorable to the enhancement of optical properties by reducing electron scattering.[15] Decreasing annealing temperature to 500 °C reduced the grain size and the formation of single NPs, because Ostwald ripening is limited at lower temperature. Increasing the loading amount of P4VP to 2 or 3 wt % enhanced the density of small GNPs formed at one site, thus promoting the generation of one large GNP through the Ostwald ripening at low annealing temperature (Figure S8). However, in this case the duration of plasma treatment needs to be optimized; otherwise, the P4VP residue caused the formation of many tiny GNPs randomly located on the substrate.

Fabrication of Other Inorganic NP and Alloying Arrays. Our method is applicable to the fabrication of intermetallic alloy arrays from different metal precursors. For metals other than Au, the thermal annealing procedures need to be optimized, depending on the type of metals and the loading amount of the metal precursors. For instance, for the Pt NP system, a one-step thermal annealing process at 800 °C is sufficient to generate monodisperse NP arrays. This is because the density of small Pt clusters at one site is much higher than that of Au clusters, due to the higher loading amount of Pt precursors on P4VP nanocylinders than that of $AuCl_4^-$ complexes. SEM images in Figure 4A–C show high-quality arrays of intermetallic Au–Pd, Fe–Pt, Co–Pt alloy NPs synthesized by using $HAuCl_4$, Na_2PdCl_4, $K_3Fe(CN)_6$, K_2PtCl_4, and $K_3Co(CN)_6$ as the precursors. The arrays had precisely arranged NPs with smooth surface and uniform shape, and did not show any defects over a large area (e.g., 100 × 100 μm^2 in Figure S9). The scanning transmission electron microscopy (STEM) images and corresponding energy-dispersive X-ray spectroscopy (EDS) show that the metal elements were uniformly distributed in the corresponding Au–Pd, Fe–Pt, and Co–Pt NPs, indicating the formation of intermetallic alloys (Figure 4D, 4F, and 4H). The atomic compositions measured from EDS were 41/59 for Au–Pd, 8/92 for Fe–Pt, and 43–57 for Co–Pt, respectively (Figure

https://doi.org/10.1021/acsnano.2c10205
ACS Nano 2023, 17, 725–734

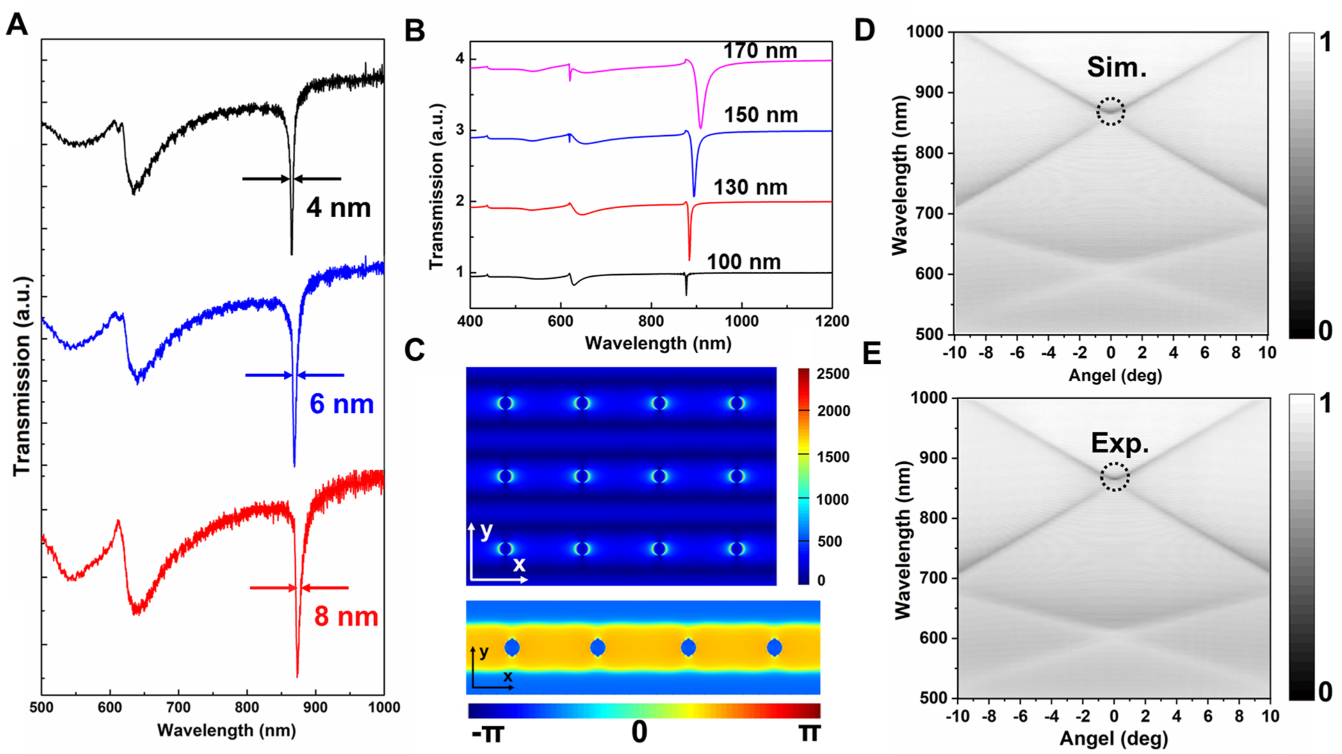

Figure 5. Optical properties of GNP square arrays. (A) Transmission spectra of the arrays with different GNP sizes: D_{NP} = 70 nm and H_{NP} = 62 nm (black line), D_{NP} = 84 nm and H_{NP} = 65 nm (blue line), D_{NP} = 94 nm and H_{NP} = 78 nm (red line). (B) Simulated transmission spectra of GNP arrays with H_{NP} = 78 nm and D_{NP} = 100, 130, 150, and 170 nm. (C) FDTD-calculated near-filed distribution map of $|E|^2$ (top) and phase map of $\Phi(E_x)$ (bottom) at band-edge lattice plasmons (λ = 870 nm, θ = 0°). (D) Simulated and (E) experimental dispersion diagrams of GNP arrays under TE polarization. Band-edge lattice modes are highlighted in the dashed circles.

S10−S12). The intermetallic structures were further confirmed by HRTEM imaging of the lattice spacing of the alloy (Figure 4E, 4G, and 4I). The measured lattice spacing of around 2.28 Å for the Au−Pd and Co−Pt alloy at ∼1:1 atomic composition indicates the formation of $L1_0$ face-centered tetragonal (fct) intermetallic structures.[39] The lattice spacing of around 2.23 Å for Fe−Pt alloy at ∼1:9 atomic composition supports the formation of $L1_2$ face-centered cubic (fcc) intermetallic structures.[29] Furthermore, our method can be used to fabricate NP arrays of other metals (e.g., Pd, Pt) and metallic oxides (Fe_2O_3, and CoO_2) (Figure S13).

Optical Properties of GNP Arrays. The transmission spectra of GNP square arrays with different diameters D_{NP} and heights H_{NP} were characterized by immersing the arrays in dimethyl sulfoxide (DMSO, n = 1.48) with refractive index matching that of the quartz (Figure 5A). We compared the optical responses of GNP square arrays with a periodicity of a_0 = 600 nm but varying diameter D_{NP}. The array with D_{NP} = 70 nm exhibited a SLR mode with full width at half-maximum (fwhm) of 4 nm at λ_{SL} = 870 nm. As D_{NP} of GNP increases to 84 and 94 nm, the peak positions of SLR red-shifted and the line widths broadened to 6 and 8 nm, respectively. This phenomenon can be explained by coupled dipole method (see detailed discussions in Supplementary Text S2),[40] in which the SLR frequency is governed by the following equations:

$$\omega_p - \frac{1}{16}\omega_p {D_{NP}}^3 \mathrm{Re}(S) \tag{3}$$

where ω_p is the surface plasmon frequency and S is the retarded dipole sum. The line width of SLR can be described as follows:

$$\mathrm{Im}(1/\alpha_s - S) \propto \frac{\omega_p {D_{NP}}^3}{\Omega} \tag{4}$$

where α_s is the polarizability of NP, and Ω is half-width of surface plasmon resonance. Thus, the main factor affecting the peak position and line width of SLR is GNP diameter rather than height (Figure S14). With the increase of GNP diameter, the frequency of SLR decreases (corresponding to SLR wavelength red shift) and the line width widens. The experiment law is consistent with our FDTD simulation of transmission spectra of the arrays of cylindrical-shaped GNPs with different diameters (Figure 5B). The maximum electric field intensity $|E|^2/|E_0|^2$ around NPs at λ_{SL} is approximately 2500, which is much larger than that around single NP at λ_{LSPR} (Figure 5C and Figure S15). The phase $\Phi(E_x)$ distribution map shows that the dipole moments of individual NPs oscillate in-phase and couple with the diffraction mode to form a standing wave pattern (Figure 5C). Experimental dispersion diagrams of GNP arrays under TE polarization showed a clear band-edge lattice mode that can support potential applications in nanolasing and sensing, which is in good agreement with our simulations (Figure 5D and 5E). The mode dispersions were reversed under TM polarization, and the out-of-plane SLRs get excited (Figure S16). The GNP hexagonal arrays show similar SLRs, and no particular advantage over square arrays in terms of the line width and near-field enhancement (Figure S17)

https://doi.org/10.1021/acsnano.2c10205
ACS Nano 2023, 17, 725−734

Table 1. Summary of Experimentally Obtained *Q*-Factors of SLR in GNP Arrays

Q	λ (nm)	material	EBL	metal deposition	thermal annealing	area	ref.
218	**870**	**GNP**	**no**	**no**	**yes**	**large**	**this work**
29	600	GNP	no	no	no	large	[42]
25	930	GNP	yes	yes	no	small	[43]
30	850	GNP	no	yes	no	large	[44]
50	600	GNP	yes	yes	no	small	[45]
60	800	GNP	yes	yes	no	small	[46]
153	764	GNP	yes	yes	no	small	[47]
300	1500	Au/Gra	yes	yes	no	small	[48]
215	860	GNP	no	yes	yes	large	[15]
2340	1550	GNP	yes	yes	no	small	[49]

CONCLUSIONS

In summary, we have developed a versatile method for fabricating high-quality inorganic NP arrays over a large area in a typical standard laboratory. This fabrication method shows at least four important advantages over existing top-down techniques: (i) it is simple to implement for efficient creation of many replicates of NP arrays at the same time from one master in a robust manner; (ii) it does not require a cleanroom facility or special tools such as electron beam lithography (EBL) and metal deposition equipment; (iii) it is applicable to fabricating NP arrays from different metals, intermetallic alloys, and metal oxides; and (iv) the resulting NPs are uniform in size and shape, and have high crystallinity and smooth surface. Table 1 summarizes the characteristic features of GNP arrays fabricated by using the state-of-the-art techniques reported in recent years. The GNP arrays prepared by our method exhibited a *Q*-factor of 218 at the wavelength 870 nm, which is the highest among all the methods capable of effectively preparing GNP arrays with an SLR wavelength range of 400–1000 nm where metals have extremely high intrinsic losses.[41] Specifically, the approach by Odom et al.[15] generates GNP arrays with a comparable *Q*-factor of 215, but requires more complicated procedures involving twice metal deposition, metal chemical etching, etc. The method we developed offers an important addition to the tools for fabricating high-quality NP arrays with tailored optical, catalytic, and magnetic properties for different applications

We envision that by changing the type of polymers, the composition of precursors, and the formation mechanism of NPs, our method can be further extended to fabricate a library of arrays from upconversion NPs,[50] quantum dots,[51] and metal–organic frameworks.[52] When relief silicon masters with nanopillars of other shapes are used, this method can be potentially used to generate arrays of shaped NPs (e.g., gold nanorods, nanotriangles). The NP arrays can be used as seeds to selectively grow a layer of other inorganic materials or as nanotemplates to guide the assembly of other NPs, yielding morphologically more complex nanostructures (e.g., core–shell or Janus structures). The diversity in the shape, composition, and morphology of NPs enables a much wider range of applications of NP arrays in such as display, lighting, imaging, and electrocatalysis.

METHODS

Materials. Metal compounds [($HAuCl_4 \cdot 3H_2O$), $K_3Fe(CN)_6$, Na_2PdCl_4, $K_3Co(CN)_6$, and K_2PtCl_4], polymer poly(4-vinylpyridine) (P4VP, average M_w ∼ 160 000), and fluorosilane (tridecafluoro-1,1,2,2-tetrahydrooctyl-1-trichlorosilane) were purchased from Sigma-Aldrich. Sulfuric acid (H_2SO_4), hydrogen peroxide (H_2O_2), hydrochloric acid (HCl), ethanol, acetone, isopropanol, and dichloromethane were purchased from Sinopharm Chemical Reagent. The relief nanopatterned silicon masters (square and hexagonal array of posts with diameter d = 250 nm and d = 190 nm, height h = 350 nm, pitch a_0 = 600 nm) were purchased from Max Levy Autograph, Inc. (MLA). All the chemicals and reagents were used as received. Deionized water used in the experiments was purified using a Millipore water purification system with a minimum resistivity of 18.2 MΩ·cm.

Preparation of the Substrate. Silicon (Si) wafers or quartz slides (1 × 1 cm^2) were sonicated in ethanol, isopropanol, and acetone for 15 min and then immersed in a 98% H_2SO_4:30% H_2O_2 = 7:3 (v/v) mixture of piranha solution. The surface was hydroxylated by boiling for 30 min, and the residual acid was removed by rinsing the Si wafers with deionized water. The wafers were dried in an oven at 100 °C for 1 h to later use.

Patterning P4VP Nanocylinders on Substrate. The relief nanopatterned silicon masters were passivated with a fluorosilane (tridecafluoro-1,1,2,2-tetrahydrooctyl-1-trichlorosilane) for 24 h in a vacuum desiccator. SYLGARD 184-PDMS (base and curing agents are mixed in 10:1 mass ratio) was poured on the masters and cured for 2 h at 70 °C. The obtained PDMS molds were placed in contact with 1 wt % P4VP isopropanol solutions for 10 s, and then the mold was immediately placed into conformal contact with the processed substrate. The solvent trapped in the wells swelled the PDMS mold and caused a reduction in size of the mold patterns. After the solvent evaporated for 30 min, the mold was removed, and P4VP posts were formed on the substrate. The diameter of the P4VP nanocylinders was tuned in the range of 120–250 nm by using solvents of different swelling factor. Although we did not focus on reducing NP dimension and interparticle spacing, previous research shows that the dimension of nanocylinders and distance between nanocylinders can be reduced down to ∼10 nm and ∼50 nm by a soft lithography-based method, respectively.[53]

Fabrication of the GNP Arrays. The patterned P4VP nanocylinders were treated by oxygen plasma at 60 mTorr, 35 s.c.c.m., and 60 W of power for 5, 10, 15, 20, and 25 s. For GNPs, the P4VP arrays were immersed in 3 mM $HAuCl_4$ acidic aqueous solution for 1 h to selectively deposit gold ionic precursors into P4VP posts. After precursor loading, the samples were rinsed with deionized water and dried with N_2 gas. Oxygen plasma treatment for 4 min completely removed the P4VP, and ordered gold nanoclusters were left on the substrate. A three-step thermal annealing protocol induced the agglomeration of gold nanoclusters and generated monodisperse GNP arrays: The temperature was first increased to 500 °C with air in 1 h followed by annealing at 500 °C for 2 h; Until it cools naturally to room temperature, the temperature was then increased to 700 °C with air in 1 h followed by annealing at 700 °C for 2 h; Until it cools naturally to room temperature, the temperature was finally increased to 1000 °C with air in 1 h followed by annealing at 1000 °C for 2 h.

Fabrication of Other Inorganic NP Arrays. For Pd and Pt NPs, the P4VP arrays were immersed in 1 mM Na_2PdCl_4:3% HCl and 1 mM K_2PtCl_4:3% HCl for 30 min. For Fe_2O_3 and CoO_2 NPs, the P4VP arrays were immersed in 1 mM $K_3Fe(CN)_6$:0.1% HCl and 1 mM $K_3Co(CN)_6$:0.1% HCl for 30 min. For AuPd alloying NP, the

P4VP arrays were immersed in 0.35 mM of Na_2PdCl_4 and 0.65 mM of $HAuCl_4$:3% HCl for 30 min. For FePt alloying NP, the P4VP arrays were immersed in 0.35 mM $K_3Fe(CN)_6$ and 0.5 mM $K_3Co(CN)_6$:3% HCl for 30 min. For CoPt alloying NP, the P4VP arrays were immersed in 0.4 mM of $K_3Co(CN)_6$ and 0.6 mM of K_2PtCl_4:3% HCl for 30 min. Subsequent thermal annealing under Ar atmospheres at 800 °C for 2 h agglomerated and crystallized nanoclusters to form NP and intermetallic nanoalloy array.

Characterization. Samples on the substrate were directly imaged using a Gemini Ultra55 (Zeiss) scanning electron microscope (SEM) or using a FEI Tecnai G2 F20 transmission electron microscope (TEM). For TEM characterization, the NP arrays on substrates were placed in ethanol and the individual NPs were peeled off from the substrates by sonication. A droplet of the NP solution in ethanol was dropped onto a TEM grid and dried in air. The surface of P4VP and GNP arrays and the film thickness were characterized using a Dimension FastScan (Bruker) atomic force microscopy. The transmission and dispersion diagram of GNP arrays were characterized by using the homemade polarization-resolved momentum-space measurement system (see detailed schematic graph in Figure S18). By using Kohler illumination, the sample was shined with different incident angles at once. The transmitted light was collected by an objective lens (N.A. = 0.4) and detected by a spectrometer at the Fourier plane. A linear polarizer was put before the spectrometer. Then the polarization-resolved dispersion diagram in wavelength (λ)-incident angle (θ) units can be obtained.

Theoretical Analysis. Please see the Supplementary Texts S1 and S2 for the detailed derivations and discussions of the nanoparticle growth model and surface lattice resonance theory.

Numerical Simulation. The optical properties, electrical field distributions, and phase maps of plasmonic structures are simulated by the finite-difference time-domain (FDTD) method (using commercial software FDTD Solutions). The angle-resolved transmittance spectra were simulated by Broadband Fixed Angle Source Technique (BFAST) in FDTD. The dielectric functions of Au are taken from the Johnson and Christy 1972 values. A uniform mesh size of 2 nm was used to ensure the accuracy of electric and magnetic field calculations within the NPs.

ASSOCIATED CONTENT

Supporting Information

The Supporting Information is available free of charge at https://pubs.acs.org/doi/10.1021/acsnano.2c10205.

Detailed model of nanoparticle growth and surface lattice resonance; Fabrication and characterization of P4VP nanocylinder arrays; Characterization of GNP arrays; Characterization of other inorganic NP arrays; Optical properties of GNP square arrays; Schematic graph of optical measurement system setup (PDF)

AUTHOR INFORMATION

Corresponding Authors

Lei Shi − *State Key Laboratory of Surface Physics, Key Laboratory of Micro- and Nano-Photonic Structures (Ministry of Education), Department of Physics, Fudan University, 200433 Shanghai, China*; Email: lshi@fudan.edu.cn

Zhihong Nie − *State Key Laboratory of Molecular Engineering of Polymers, Department of Macromolecular Science, Fudan University, 200433 Shanghai, China; Yiwu Research Institute of Fudan University, 322000 Yiwu, China*; orcid.org/0000-0001-9639-905X; Email: znie@fudan.edu.cn

Authors

Fan Yang − *State Key Laboratory of Molecular Engineering of Polymers, Department of Macromolecular Science, Fudan University, 200433 Shanghai, China*; orcid.org/0000-0002-9395-5310

Qianyun Chen − *State Key Laboratory of Molecular Engineering of Polymers, Department of Macromolecular Science, Fudan University, 200433 Shanghai, China*

Jiajun Wang − *State Key Laboratory of Surface Physics, Key Laboratory of Micro- and Nano-Photonic Structures (Ministry of Education), Department of Physics, Fudan University, 200433 Shanghai, China*; orcid.org/0000-0002-7554-370X

Julia J. Chang − *State Key Laboratory of Molecular Engineering of Polymers, Department of Macromolecular Science, Fudan University, 200433 Shanghai, China*

Wenhao Dong − *State Key Laboratory of Molecular Engineering of Polymers, Department of Macromolecular Science, Fudan University, 200433 Shanghai, China*

Wei Cao − *State Key Laboratory of Molecular Engineering of Polymers, Department of Macromolecular Science, Fudan University, 200433 Shanghai, China*; orcid.org/0000-0001-7578-0900

Shunsheng Ye − *State Key Laboratory of Molecular Engineering of Polymers, Department of Macromolecular Science, Fudan University, 200433 Shanghai, China*

Complete contact information is available at: https://pubs.acs.org/10.1021/acsnano.2c10205

Author Contributions

‖F.Y. and Q.C. contributed equally to this work. F.Y., Q.C., J.C., and Z.N. conceived the idea. F.Y. performed the theoretical analysis. F.Y. and J.W. carried out the numerical simulation and the measurements. F.Y. and Q.C. fabricated the samples. W.D., W.C., and S.Y. took part in discussions and analysis. L.S. and Z.N. supervised the project. F.Y. and Q.C. wrote the manuscript. All authors contributed to the manuscript and approved the final version.

Notes

The authors declare no competing financial interest.

ACKNOWLEDGMENTS

We acknowledge the financial support from the Innovation Program of Shanghai Municipal Education Commission (2021-01-07-00-07-E00073), and the National Natural Science Foundation of China (Grants 5210030633, 52125308, 91963107, 51973038). The authors thank Hongtao Xu, Longfei Lv, and Chunyu Cui for their support on fabrication and characterization, Liwei Dai for fruitful discussions, and the Nanofabrication Lab at Fudan University and Ideaoptics Technology Ltd., China for facility support.

REFERENCES

(1) Nie, Z.; Petukhova, A.; Kumacheva, E. Properties and emerging applications of self-assembled structures made from inorganic nanoparticles. *Nat. Nanotechnol.* **2010**, *5* (1), 15−25.

(2) Halas, N. J.; Lal, S.; Chang, W.-S.; Link, S.; Nordlander, P. Plasmons in Strongly Coupled Metallic Nanostructures. *Chem. Rev.* **2011**, *111* (6), 3913−3961.

(3) Giner-Casares, J. J.; Henriksen-Lacey, M.; Coronado-Puchau, M.; Liz-Marzán, L. M. Inorganic nanoparticles for biomedicine: where materials scientists meet medical research. *Mater. Today* **2016**, *19* (1), 19−28.

(4) Liu, W.; Tagawa, M.; Xin, H. L.; Wang, T.; Emamy, H.; Li, H.; Yager, K. G.; Starr, F. W.; Tkachenko, A. V.; Gang, O. Diamond

family of nanoparticle superlattices. *Science* **2016**, *351* (6273), 582−586.

(5) Zhang, H.; Kinnear, C.; Mulvaney, P. Fabrication of Single-Nanocrystal Arrays. *Adv. Mater.* **2020**, *32* (18), 1904551.

(6) Hu, M.; Chen, J.; Li, Z.-Y.; Au, L.; Hartland, G. V.; Li, X.; Marquez, M.; Xia, Y. Gold nanostructures: engineering their plasmonic properties for biomedical applications. *Chem. Soc. Rev.* **2006**, *35* (11), 1084−1094.

(7) Jain, P. K.; Huang, X. H.; El-Sayed, I. H.; El-Sayed, M. A. Noble Metals on the Nanoscale: Optical and Photothermal Properties and Some Applications in Imaging, Sensing, Biology, and Medicine. *Acc. Chem. Res.* **2008**, *41* (12), 1578−1586.

(8) Gong, S.; Schwalb, W.; Wang, Y.; Chen, Y.; Tang, Y.; Si, J.; Shirinzadeh, B.; Cheng, W. A wearable and highly sensitive pressure sensor with ultrathin gold nanowires. *Nat. Commun.* **2014**, *5* (1), 3132.

(9) Neubrech, F.; Duan, X.; Liu, N. Dynamic plasmonic color generation enabled by functional materials. *Sci. Adv.* **2020**, *6* (36), No. eabc2709.

(10) Yang, F.; Ye, S.; Dong, W.; Zheng, D.; Xia, Y.; Yi, C.; Tao, J.; Sun, C.; Zhang, L.; Wang, L.; et al. Laser-Scanning-Guided Assembly of Quasi-3D Patterned Arrays of Plasmonic Dimers for Information Encryption. *Adv. Mater.* **2021**, *33* (24), 2100325.

(11) Zhou, L.; Swearer, D. F.; Zhang, C.; Robatjazi, H.; Zhao, H.; Henderson, L.; Dong, L.; Christopher, P.; Carter, E. A.; Nordlander, P.; et al. Quantifying hot carrier and thermal contributions in plasmonic photocatalysis. *Science* **2018**, *362* (6410), 69−72.

(12) Kauranen, M.; Zayats, A. V. Nonlinear plasmonics. *Nat. Photonics* **2012**, *6* (11), 737−748.

(13) Kravets, V. G.; Kabashin, A. V.; Barnes, W. L.; Grigorenko, A. N. Plasmonic Surface Lattice Resonances: A Review of Properties and Applications. *Chem. Rev.* **2018**, *118* (12), 5912−5951.

(14) Cherqui, C.; Bourgeois, M. R.; Wang, D.; Schatz, G. C. Plasmonic Surface Lattice Resonances: Theory and Computation. *Acc. Chem. Res.* **2019**, *52* (9), 2548−2558.

(15) Deng, S.; Li, R.; Park, J.-E.; Guan, J.; Choo, P.; Hu, J.; Smeets, P. J. M.; Odom, T. W. Ultranarrow plasmon resonances from annealed nanoparticle lattices. *Proc. Natl. Acad. Sci. U.S.A.* **2020**, *117* (38), 23380−23384.

(16) Lee, S. A.; Link, S. Chemical Interface Damping of Surface Plasmon Resonances. *Acc. Chem. Res.* **2021**, *54* (8), 1950−1960.

(17) Zhou, W.; Odom, T. W. Tunable subradiant lattice plasmons by out-of-plane dipolar interactions. *Nat. Nanotechnol.* **2011**, *6* (7), 423−427.

(18) Zou, S.; Janel, N.; Schatz, G. C. Silver nanoparticle array structures that produce remarkably narrow plasmon lineshapes. *J. Chem. Phys.* **2004**, *120* (23), 10871−10875.

(19) Zhang, H.; Cadusch, J.; Kinnear, C.; James, T.; Roberts, A.; Mulvaney, P. Direct Assembly of Large Area Nanoparticle Arrays. *ACS Nano* **2018**, *12* (8), 7529−7537.

(20) Flauraud, V.; Mastrangeli, M.; Bernasconi, G. D.; Butet, J.; Alexander, D. T. L.; Shahrabi, E.; Martin, O. J. F.; Brugger, J. Nanoscale topographical control of capillary assembly of nanoparticles. *Nat. Nanotechnol.* **2017**, *12* (1), 73−80.

(21) Lin, Q.-Y.; Mason, J. A.; Li, Z.; Zhou, W.; O'Brien, M. N.; Brown, K. A.; Jones, M. R.; Butun, S.; Lee, B.; Dravid, V. P.; et al. Building superlattices from individual nanoparticles via template-confined DNA-mediated assembly. *Science* **2018**, *359* (6376), 669−672.

(22) Ye, S.; Zha, H.; Xia, Y.; Dong, W.; Yang, F.; Yi, C.; Tao, J.; Shen, X.; Yang, D.; Nie, Z. Centimeter-Scale Superlattices of Three-Dimensionally Orientated Plasmonic Dimers with Highly Tunable Collective Properties. *ACS Nano* **2022**, *16* (3), 4609−4618.

(23) Ng, K. C.; Udagedara, I. B.; Rukhlenko, I. D.; Chen, Y.; Tang, Y.; Premaratne, M.; Cheng, W. Free-Standing Plasmonic-Nanorod Superlattice Sheets. *ACS Nano* **2012**, *6* (1), 925−934.

(24) Si, K. J.; Sikdar, D.; Chen, Y.; Eftekhari, F.; Xu, Z.; Tang, Y.; Xiong, W.; Guo, P.; Zhang, S.; Lu, Y.; et al. Giant Plasmene Nanosheets, Nanoribbons, and Origami. *ACS Nano* **2014**, *8* (11), 11086−11093.

(25) Yang, K.; Yao, X.; Liu, B.; Ren, B. Metallic Plasmonic Array Structures: Principles, Fabrications, Properties, and Applications. *Adv. Mater.* **2021**, *33* (50), 2007988.

(26) Lee, M. H.; Huntington, M. D.; Zhou, W.; Yang, J.-C.; Odom, T. W. Programmable Soft Lithography: Solvent-Assisted Nanoscale Embossing. *Nano Lett.* **2011**, *11* (2), 311−315.

(27) Yang, A. K.; Hoang, T. B.; Dridi, M.; Deeb, C.; Mikkelsen, M. H.; Schatz, G. C.; Odom, T. W. Real-time tunable lasing from plasmonic nanocavity arrays. *Nat. Commun.* **2015**, *6*, 6939.

(28) Cha, S. K.; Mun, J. H.; Chang, T.; Kim, S. Y.; Kim, J. Y.; Jin, H. M.; Lee, J. Y.; Shin, J.; Kim, K. H.; Kim, S. O. Au-Ag Core-Shell Nanoparticle Array by Block Copolymer Lithography for Synergistic Broadband Plasmonic Properties. *ACS Nano* **2015**, *9* (5), 5536−5543.

(29) Mun, J. H.; Chang, Y. H.; Shin, D. O.; Yoon, J. M.; Choi, D. S.; Lee, K.-M.; Kim, J. Y.; Cha, S. K.; Lee, J. Y.; Jeong, J.-R.; et al. Monodisperse Pattern Nanoalloying for Synergistic Intermetallic Catalysis. *Nano Lett.* **2013**, *13* (11), 5720−5726.

(30) Chai, J.; Wang, D.; Fan, X.; Buriak, J. M. Assembly of aligned linear metallic patterns on silicon. *Nat. Nanotechnol.* **2007**, *2* (8), 500−506.

(31) Huang, L. L.; Shen, B.; Lin, H. X.; Shen, J. H.; Jibril, L.; Zheng, C. Y.; Wolverton, C.; Mirkin, C. A. Regioselective Deposition of Metals on Seeds within a Polymer Matrix. *J. Am. Chem. Soc.* **2022**, *144* (11), 4792−4798.

(32) Ma, J.; Hu, J. M.; Li, Z.; Nan, C. W. Recent Progress in Multiferroic Magnetoelectric Composites: from Bulk to Thin Films. *Adv. Mater.* **2011**, *23* (9), 1062−1087.

(33) Deng, S.; Zhang, B.; Choo, P.; Smeets, P. J. M.; Odom, T. W. Plasmonic Photoelectrocatalysis in Copper-Platinum Core-Shell Nanoparticle Lattices. *Nano Lett.* **2021**, *21* (3), 1523−1529.

(34) Khorasaninejad, M.; Chen, W. T.; Devlin, R. C.; Oh, J.; Zhu, A. Y.; Capasso, F. Metalenses at visible wavelengths: Diffraction-limited focusing and subwavelength resolution imaging. *Science* **2016**, *352* (6290), 1190−1194.

(35) Shin, D. O.; Lee, D. H.; Moon, H.-S.; Jeong, S.-J.; Kim, J. Y.; Mun, J. H.; Cho, H.; Park, S.; Kim, S. O. Sub-Nanometer Level Size Tuning of a Monodisperse Nanoparticle Array Via Block Copolymer Lithography. *Adv. Funct. Mater.* **2011**, *21* (2), 250−254.

(36) Xu, L.; Liang, H.-W.; Yang, Y.; Yu, S.-H. Stability and Reactivity: Positive and Negative Aspects for Nanoparticle Processing. *Chem. Rev.* **2018**, *118* (7), 3209−3250.

(37) Wynblatt, P.; Gjostein, N. A. Particle growth in model supported metal catalysts—I. Theory. *Acta Metall.* **1976**, *24* (12), 1165−1174.

(38) Anderoglu, O.; Misra, A.; Wang, H.; Zhang, X. Thermal stability of sputtered Cu films with nanoscale growth twins. *J. Appl. Phys.* **2008**, *103* (9), 094322.

(39) Liou, S. H.; Huang, S.; Klimek, E.; Kirby, R. D.; Yao, Y. D. Enhancement of coercivity in nanometer-size CoPt crystallites. *J. Appl. Phys.* **1999**, *85* (8), 4334−4336.

(40) Zou, S.; Janel, N.; Schatz, G. C. Silver nanoparticle array structures that produce remarkably narrow plasmon lineshapes. *J. Chem. Phys.* **2004**, *120* (23), 10871−10875.

(41) Khurgin, J. B. How to deal with the loss in plasmonics and metamaterials. *Nat. Nanotechnol.* **2015**, *10* (1), 2−6.

(42) Vinnacombe-Willson, G. A.; Conti, Y.; Jonas, S. J.; Weiss, P. S.; Mihi, A.; Scarabelli, L. Surface Lattice Plasmon Resonances by Direct In Situ Substrate Growth of Gold Nanoparticles in Ordered Arrays. *Adv. Mater.* **2022**, *34* (37), 2205330.

(43) Chu, Y.; Schonbrun, E.; Yang, T.; Crozier, K. B. Experimental observation of narrow surface plasmon resonances in gold nanoparticle arrays. *Appl. Phys. Lett.* **2008**, *93* (18), 181108.

(44) Rodriguez, S. R. K.; Abass, A.; Maes, B.; Janssen, O. T. A.; Vecchi, G.; Rivas, J. G. Coupling Bright and Dark Plasmonic Lattice Resonances. *Phys. Rev. X* **2011**, *1* (2), 021019.

(45) Kravets, V. G.; Schedin, F.; Grigorenko, A. N. Extremely narrow plasmon resonances based on diffraction coupling of localized

plasmons in arrays of metallic nanoparticles. *Phys. Rev. Lett.* **2008**, *101* (8), 087403.

(46) Auguie, B.; Barnes, W. L. Collective resonances in gold nanoparticle arrays. *Phys. Rev. Lett.* **2008**, *101* (14), 143902.

(47) Kravets, V. G.; Schedin, F.; Kabashin, A. V.; Grigorenko, A. N. Sensitivity of collective plasmon modes of gold nanoresonators to local environment. *Opt. Lett.* **2010**, *35* (7), 956−958.

(48) Thackray, B. D.; Thomas, P. A.; Auton, G. H.; Rodriguez, F. J.; Marshall, O. P.; Kravets, V. G.; Grigorenko, A. N. Super-Narrow, Extremely High Quality Collective Plasmon Resonances at Telecom Wavelengths and Their Application in a Hybrid Graphene-Plasmonic Modulator. *Nano Lett.* **2015**, *15* (5), 3519−3523.

(49) Bin-Alam, M. S.; Reshef, O.; Mamchur, Y.; Alam, M. Z.; Carlow, G.; Upham, J.; Sullivan, B. T.; Menard, J.-M.; Huttunen, M. J.; Boyd, R. W.; Dolgaleva, K.; et al. Ultra-high-Q resonances in plasmonic metasurfaces. *Nat. Commun.* **2021**, *12* (1), 974.

(50) Wu, Y.; Xu, J.; Poh, E. T.; Liang, L.; Liu, H.; Yang, J. K. W.; Qiu, C.-W.; Vallée, R. A. L.; Liu, X. Upconversion superburst with sub-2 μs lifetime. *Nat. Nanotechnol.* **2019**, *14* (12), 1110−1115.

(51) Zhang, D.; Zhang, Q.; Ren, B.; Zhu, Y.; Abdellah, M.; Fu, Y.; Cao, B.; Wang, C.; Gu, L.; Ding, Y.; et al. Large-scale planar and spherical light-emitting diodes based on arrays of perovskite quantum wires. *Nat. Photonics* **2022**, *16* (4), 284−290.

(52) Duan, J.; Chen, S.; Zhao, C. Ultrathin metal-organic framework array for efficient electrocatalytic water splitting. *Nat. Commun.* **2017**, *8* (1), 15341.

(53) Shim, W.; Braunschweig, A. B.; Liao, X.; Chai, J.; Lim, J. K.; Zheng, G.; Mirkin, C. A. Hard-tip, soft-spring lithography. *Nature* **2011**, *469* (7331), 516−520.